Journal of Environmental Chemical Engineering 11 (2023) 110415

Contents lists available at ScienceDirect

Journal of Environmental Chemical Engineering

journal homepage: www.elsevier.com/locate/jece

Solar photocatalytic degradation of polyethylene terephthalate nanoplastics: Evaluation of the applicability of the TiO_2/MIL-100(Fe) composite material

C.A. Rojas-Guerrero [a], M. Villanueva-Rodríguez [a], J.L. Guzmán-Mar [a], A. Hernández-Ramírez [a], E.I. Cedillo-González [b], F.E. Longoria Rodríguez [c], L. Hinojosa-Reyes [a,*]

[a] Universidad Autónoma de Nuevo León (UANL), Facultad de Ciencias Químicas, Ave. Universidad s/n, San Nicolás de los Garza, C.P. 66455, Nuevo León, Mexico
[b] University of Modena and Reggio Emilia, Department of Engineering, "Enzo Ferrari", Via Vivarelli 10, 41125 Modena, Italy
[c] Centro de Investigación en Materiales Avanzados S.C., Unidad Monterrey, Alianza Norte 202, Apodaca C.P. 66628, Nuevo León, Mexico

ARTICLE INFO

Editor: Despo Kassinos

Keywords:
TiO_2 based composite
Iron-containing metal organic framework
Photocatalysis
Polyethylene terephthalate
Nanoplastics degradation

ABSTRACT

For the first time, TiO_2/MIL-100(Fe) photocatalysts supported on perlite mineral particles prepared by the solvothermal/microwave methods and post-annealing technique were tested in the degradation of polyethylene terephthalate nanoplastics (PET NPs). Powder X-ray diffraction, Fourier transform infrared spectroscopy, thermogravimetric analysis, scanning electron microscopy, X-ray photoelectron spectroscopy, UV–vis diffuse reflectance spectroscopy, N_2 physisorption, photoluminescence emission spectroscopy, photocurrent response, and electrochemical impedance spectroscopy were used to characterize the as-prepared materials. The response surface methodology approach was used to study the effects: pH of the NPs suspension and incorporated amount of MIL-100(Fe) on the TiO_2/MIL-100(Fe) catalyst to optimize the photocatalytic degradation of the PET NPs under simulated solar light. The degradation of the PET NPs was evaluated by measuring turbidity and carbonyl index (FTIR) changes. The total organic carbon (TOC) in the solution during the degradation of the PET NPs was assessed to measure NPs oxidation into water-soluble degradation by-products. The active species involved in the photocatalytic degradation of PET NPs by the TiO_2/MIL-100(Fe) composite was further examined based on trapping experiments. The use of 12.5 wt% TiO_2/MIL-100(Fe) catalyst showed improved photocatalytic efficacy in the oxidation of PET NPs at pH 3 under simulated sunlight compared to bare TiO_2. The increase in the carbonyl index (CI = 0.99), the reduction in the turbidity ratio (0.454), and the increase in the content of TOC released (3.00 mg/L) were possible with 12.5 wt% TiO_2/MIL-100(Fe) material. In contrast, the PET NPs were slowly degraded by TiO_2-based photocatalysis (CI = 0.96, turbidity ratio = 0.539, released TOC = 2.12 mg/L). The mesoporous TiO_2/MIL-100(Fe) composites with high specific surface area, capacity to absorb visible light, and effective separation of photogenerated electron-hole charges clearly demonstrated the enhancement of the photocatalytic performance in the PET NPs degradation under simulated solar light.

1. Introduction

One of the most prevalent polymers in the aquatic environment and in the influent and effluent of wastewater treatment plants (WWTPs) is polyethylene terephthalate (PET) [1–3]. PET, a thermoplastic polymer from the polyester family, is produced by reacting ethylene glycol and terephthalic acid at high temperatures and low vacuum pressures. PET is a versatile material frequently used to produce bottles, food containers, and synthetic fibers due to its transparency, flexibility, low density, strong chemical resistance, and low cost [2]. The worldwide production of PET in 2017 was 30.3 million tons [4]. Plastics are accumulated in the environment due to improper disposal and resistance to degradation. The plastics accumulated in the environment can be fragmented by abiotic actions such as solar radiation or mechanics, resulting in the so-called microplastics (MPs, <5 mm) and nanoplastics (NPs, <1 μm). MPs and NPs are an issue of global concern in the marine environment [3,5]. NPs are emerging pollutants that have attracted much attention due to their stable nature, negligible degradation, and high permeability

* Correspondence to: Laura Hinojosa-Reyes, Universidad Autónoma de Nuevo León, Mexico.
E-mail address: laura.hinojosary@uanl.edu.mx (L. Hinojosa-Reyes).

https://doi.org/10.1016/j.jece.2023.110415
Received 19 February 2023; Received in revised form 18 June 2023; Accepted 21 June 2023
Available online 22 June 2023

to human and animal tissues, leading to metabolic disorders and local inflammation [5]. Heterogeneous photocatalysis (HP) has become a promising treatment technology for removing MPs and NPs in water because of its operability, high efficiency, and low cost [1,6]. In HP, electrons (e^-) from the valence band (VB) are induced into the conduction band (CB), leaving holes (h^+) in the VB when a semiconductor is excited with light of an appropriate wavelength. When the photogenerated e^- and h^+ react with dissolved O_2 and H_2O respectively, produce highly reactive oxygen species like hydroxyl (•OH) and superoxide ($O_2^{\bullet-}$) radicals that can participate in the degradation of organic contaminants to generate less toxic compounds and eventually mineralize them into CO_2 and H_2O [7]. The photocatalytic degradation of MPs and NPs depends on several critical factors such as plastic properties (particle size, color, surface morphology, hydrophilicity, crystallinity, particle size) and pH value [8,9]. NPs are degraded more readily than MPs because the reactivity of •OH is increased at smaller particle sizes and bigger plastic surfaces [9]. Photocatalytic degradation of polystyrene (PS) NPs at pH 6.3 using TiO_2-P25/β-SiC foam under UV-A radiation (60 W/m^2; λmax= 365 nm). was enhanced by reducing the NPs size from 508 to 140 nm, showing 50% mineralization within 7 h [10]. Jiang et al. [11] also drew a similar conclusion, who successfully degraded tiny high-density (200–250 μm) polyethylene MPs under visible light using a hydroxyl-rich BiOCl photocatalyst with a mass loss of 5.38% within 5 h. Other applications of the photocatalytic degradation of PS NPs (<1 μm) have been demonstrated by using immobilized TiO_2 with a multilayer structure which demonstrated 23.5% elimination under UV irradiation [12] and 18–23% degradation efficiency using immobilized Cu_2O/CuO materials under visible light [13]. Recent studies have reported slow photocatalytic decomposing of fiber-based PET microplastics using Bi_2O_3@N-TiO_2 heterojunction [14] and N-doped TiO_2 nanoflowers decorated with Pt nanoparticles [15] using a Xe lamp as the light source. The degradation efficiencies of 10.2 and 5.8% as weight loss obtained with these catalysts after 48 h of reaction were attributed to PET surface oxidation by the photocatalytic process.

Titanium dioxide (TiO_2) is the most widely used photocatalyst for environmental applications; however, it is characterized by its large band gap (Eg=3.2 eV) and high recombination rate of photoexcited e^-/h^+ pairs. Coupling TiO_2 with other materials is a strategy to reduce the Eg of TiO_2, increase visible light absorption, and separate photoexcited carriers [7,16,17]. Metal-organic frameworks (MOFs) that consist of metal clusters and organic linkers [16] are attractive photocatalytic materials [16,18]. MOF metal-oxo clusters can be viewed as semiconductor quantum devices, and organic coordinating ligands are antennas that absorb light and transfer photoexcited electrons to the metal clusters through a ligand-metal charge transfer (LMCT) mechanism. TiO_2 acts as the primary catalyst in the composite structure, and the MOF, the co-catalyst, is a platform for transporting photogenerated electrons [16,17,19]. Among the several MOFs, MIL-100(Fe) from the MIL family (Materieux de l'Institut Lavoisier), which comprises Fe(III) metal centers linked with 1,3,5-benzene tricarboxylic acid (trimesic acid), demonstrates favorable features, including mesoporous voids, large surface area, suitable HOMO-LUMO gap (1.80–2.12 eV) with a visible light photocatalytic response, high chemical and aqueous stability, and low toxicity [20,21]. The MIL-100(Fe) is usually prepared by the hydrothermal method with reaction times between 12 and 70 h and temperatures between 130 and 150 °C [20,22], or by stirring the reaction mixture mechanically for 12 h at room temperature [23]. MIL-100 (Fe) with TiO_2 composites have shown higher photocatalytic effectiveness in pollutant degradation compared with the individual components [20,22,23]. TiO_2/MIL-100(Fe) microspheres prepared by the layer-by-layer method showed enhanced photocatalytic performance in the methylene blue (MB) degradation under visible light achieving 87% mineralization within 120 min [20]. The MIL-100(Fe) loaded on N-doped TiO_2 nanoparticles achieved 99.1 and 93.5% removal of MB and rhodamine B dyes within 180 min under visible light [22]. Some examples of TiO_2 composites combined with other iron-based MOFs for degrading emerging pollutants have also been reported. For instance, Liu et al. [23] evaluated the performance of TiO_2/MIL-101(Fe) magnetic composites prepared by the solvothermal method, followed by annealing at 350 °C in the degradation of tetracycline under sunlight, achieving 92.76% of efficiency within 10 min. In the present work was reported a new method for synthesizing a TiO_2/MIL-100(Fe) photocatalyst by combining the microwave-assisted MIL-100(Fe) method with the solvothermal synthesis of the composite, followed by a post-annealing thermal treatment. The TiO_2/MIL-100(Fe) photocatalytic activity was evaluated in the degradation of PET NPs. The immobilization of the catalyst represents a great opportunity to increase the performance and recyclability of the catalyst and allow a straightforward assessment of the PET NPs degradation. For instance, the photocatalytic removal of NPs was evaluated by using nanocomposite films made of N-TiO_2 [24], ZnO nanorods produced on glass substrates [25], and TiO_2 [12] and Cu_2O/CuO [13] immobilized on metal surfaces. The perlite mineral particles were proposed in this study as an option for immobilizing the TiO_2-based photocatalysts due to their large porosity [26]. Therefore, this work deals with a facile method to synthesize MIL-100(Fe) anchored with TiO_2 photocatalysts and then supported on perlite particles. The performance of the as-prepared catalyst was tested for the first time to degrade PET NPs in aqueous suspension under simulated sunlight. The PET NPs degradation was assessed by considering the evolution of the carbonyl index in FTIR, the turbidity measurements, and water-soluble by-products formed during the degradation process, which were indirectly measured by TOC analysis.

2. Methods

2.1. Materials and reagents

All the chemicals were of analytical reagent grade and utilized without additional purification. Trifluoroacetic acid (TFA, > 99% purity), sodium dodecyl sulfate (SDS, ≥ 99% purity), ferric (III) chloride hexahydrate ($FeCl_3$ 6 H_2O, ≥ 98% purity), 1,3,5-benzene tricarboxylic acid (trimesic acid, ≥ 98% purity), barium sulfate (99% purity), titanium isopropoxide (97% purity), 2-propanol (2-PrOH, 99% purity) and tert-butanol (t-BuOH, 99% purity) were purchased from Sigma-Aldrich. Ethanol (99.6% purity), hydrochloric acid (37.4%), hydrofluoric acid (49.7%), isopropanol (99.9% purity), nitric acid (65.2%), and sulfuric acid (95–96%) were from Desarrollo de Especialidades Químicas S.A. de C.V. Potassium bromide (99.9% purity), and sodium hydroxide (98.6% purity) were from Baker and CTR Scientific, respectively. Perlite mineral granules (diameter 2 mm, composition SiO_2 67%, Al_2O_3 13%, Na_2O 6%, K_2O 5%, and CaO < 5%) were supplied by Termolita.

2.2. Preparation of PET nanoplastics

According to a previous report, PET-NPs were obtained from commercially available water-plastic bottles [27]. The PET bottle was cut into small pieces (1 cm × 1 cm), and then, 1 g of PET sample was dissolved in 10 mL of 90% v/v TFA at 50 °C and stirred for 2 h until it was completely dissolved. The solution was then kept at room temperature overnight. The micro/nanoplastics were precipitated by adding 10 mL of 20% v/v TFA to the solution and stirring for 2 h. After the precipitation was completed, the supernatant liquid was discarded. The pellet was suspended in 100 mL of 0.5% w/v SDS solution, stirred vigorously for 15 min, and sonicated for 1 h. The plastics were then placed in a 100 mL test tube for 1 h; after collecting the top 50 mL suspension, it was washed with water three times to remove the residual SDS and dried at 80 °C. The collected white solid was stored until analysis.

2.3. TiO_2/MIL-100(Fe) synthesis

The MIL-100(Fe) material was prepared according to a previously

reported method [28] with slight modifications using a microwave-assisted heating process (supplementary information, **SI**). TiO_2/MIL-100(Fe) composites with 5, 12.5, and 20 wt% of MIL-100(Fe) were synthesized by the solvothermal method [29]. Briefly, 2.4×10^{-4}, 6.1×10^{-4}, or 9.7×10^{-4} moles of MIL-100(Fe) were dispersed in 40 mL of ethanol, then 8 mL of titanium (IV) isopropoxide were added and stirred for 1 h. 20 mL of ethanol and 8 mL of 1 M HCl were added dropwise to this suspension and stirred for 1 h. The resulting mixture was transferred to a 100-mL Teflon-lined stainless-steel autoclave and heated for 12 h at 180 °C. The solid was calcined in an air muffle furnace at 350 °C for 2 h. Bare TiO_2 was synthesized under the same conditions without adding MIL-100(Fe). TiO_2/MIL-100(Fe) was supported on perlite granules using the preparation method previously described [30, 31]. Briefly, the TiO_2/MIL-100(Fe) dispersion was prepared using 0.6 g of catalyst added to 15 mL of isopropanol. The mixture was sonicated for 30 min, then 6 μL of concentrated HNO_3 were added and sonicated for 30 min 1 g of perlite granules (>2 mm mesh size) were pre-washed 3 times with water and then heated in a muffle furnace at 350 °C for 30 min. Perlite was then gently stirred on the catalyst dispersion for 1 h, dried at 80 °C for 8 h, and thermally treated at 350 °C for 30 min

2.4. Characterizations

The morphology and particle size of the PET NPs were evaluated by scanning electron microscopy (JEOL JSM 6701 F) in secondary electron imaging mode at a voltage of 8.0 kV and a magnification of 50,000X. Samples were dispersed in isopropanol and placed in aluminum foil for analysis. The functional groups of the PET-NPs were identified using Fourier transform infrared spectroscopy (FTIR) on a Shimadzu IRAffinity-1 spectrophotometer with samples diluted to 0.5 wt% using KBr.

Different instrumental techniques were used to characterize the TiO_2/MIL-100(Fe) catalysts. The MIL-100(Fe) was subjected to the thermogravimetric analysis on a SDT Q600 V20.9 Build 20 thermogravimetric instrument at a heating rate of 10 °C/min from 25° to 700 °C and a N_2 flow rate of 50 mL/min. Scanning electron microscopy (JEOL JSM 6701 F) operating in secondary electron imaging mode at a voltage of 8.0 kV and a magnification of 50,000X was applied to characterize the morphology of the prepared photocatalysts. Elemental composition was investigated by energy-dispersive X-ray spectroscopy using a scanning electron microscope (JEOL JSM 6701 F) in secondary electron imaging mode at a voltage of 8.0 kV. The iron content in the TiO_2/MIL-100(Fe) catalysts was determined using a SpectrAA-220 Atomic absorption spectrometer (Varian). Varian SpectrAA 220 at. absorption spectrometer. The catalysts were digested in 1 mL HF, 3 mL HNO_3, and 1 mL HCl at 180 °C by microwave-assisted digestion for 20 min. The X-ray powder diffraction pattern of the solid was measured on a Bruker AXS D2 Phaser diffractometer using a Cu (Cu kα λ = 1.5418 Å) radiation anode operating in the 2θ range from 5° to 90°. The average crystal size was calculated by applying the Scherrer equation to the (101) diffraction peak of anatase TiO_3, The adsorption-desorption isotherms were obtained using a nitrogen adsorption-desorption instrument (Micromeritics Tristar II 3020) at − 196 °C. Following a 12-hour degassing period at 150 °C, the samples were measured. The specific surface area and pore size distribution were calculated by the Brunauer-Emmett-Teller (BET) method and the Barrett-Joyner-Halenda (BJH) method, respectively.

Fourier transform infrared spectrophotometry (Shimadzu IRAffinity-1 spectrophotometer) was used to identify functional groups in materials. To prepare the KBr pellets, 0.5 mg of powdered material was combined with 99.5 mg of KBr in an agate mortar. UV–vis diffuse reflectance (DRS) spectra of powder samples were recorded in the 200–700 nm range on a Nicolet Evolution 300 UV-Vis Spectrophotometer (Thermo Fischer Scientific) equipped with the TFS mantis accessory. $BaSO_4$ was used for background correction. The band gap of the materials was calculated using the Kubelka-Munk method. The photoluminescence (PL) emission spectra of the powdered catalysts at 315 nm excitation wavelength were recorded using a Perkin Elmer UV-Vis fluorescence spectrometer (model LS-55). The surface electronic states of the materials were investigated using X-ray photoelectron spectroscopy (XPS, K-Alpha, Thermo Fischer Scientific) using a monochromatic Al-Kα radiation source of 1486.6 eV. The binding energies were calibrated to the main peak of C1s at 284.6 eV. A three-electrode configuration with a BASi Epsilon potentiostat consisting of a Pt plate as the counter electrode and Ag/AgCl as the reference electrode was used to conduct the electrochemical experiments. The working electrode was prepared with 30 mg of catalyst combined with 400 μL of Nafion® and 600 μL of ethanol, and stirred for 30 min in an ultrasonic bath. The mixture was deposited onto FTO glass (1.96 cm^2 active area) using the drop-casting technique, and then it was dried at 70 °C for 60 min. The experiments were conducted in a 125 cm^3 quartz cell with a 0.5 M Na_2SO_4 aqueous solution as a supporting electrolyte.

During the transient photocurrent response testing, a 300-W Xe lamp with a cut-off filter (300–1100 nm) was employed as the light source.

The TiO_2/MIL-100(Fe) supported on perlite mineral particles was characterized by the SEM/EDS and XRD techniques.

2.5. Photocatalytic experiments

The as-prepared TiO_2/MIL-100(Fe) was used in the photocatalytic degradation of PET NPs under simulated sunlight. The photocatalytic experiments were carried out in a batch reactor (200 mL) containing 100 mg/L of PET NPs in water suspension (pre-sonicated for 30 min). First, the PET NPs suspension was adjusted to the desired pH value with 1 M H_2SO_4 or 0.1 M NaOH. The supported catalyst (0.125 g/L catalyst loading) was immobilized inside the reactor in a fine mesh stainless steel basket (4.2 ×4.2 ×4.4 cm). The PET NPs suspension was irradiated with an Atlas Sun Test XLS+ solar simulator (Xe lamp 300–800 nm) at an intensity of 30 W/m^2 (5-h reaction time). Samples were taken every 100 kJ/m^2 until the accumulated UV energy reached 600 kJ/m^2. The turbidity of the samples collected during the photocatalytic reaction was analyzed (portable nephelometer Lovibond TB 250 WL). FTIR spectroscopy was used to analyze the PET NPs in KBr pellets before and after the photocatalytic reaction. The carbonyl index (CI) was used to determine the degree of oxidation. The CI was calculated from the ratio of absorbance at 1710 cm^{-1} (carbonyl, C═O) and 1508 cm^{-1} (aromatic, C═C) peak heights [32]. The content of total organic carbon (TOC) resulting from the water-soluble degradation by-products generated during the photocatalytic reaction was determined in the filtered solution (Phenex RC 0.45 μm syringe filter) using a TOC analyzer (TOC-V CSH, Shimadzu).

The response surface methodology using the face-centered central composite design was chosen to determine the influence of the following two factors: 1) incorporated amount of MIL-100(Fe) in the TiO_2 photocatalyst (5, 12.5, and 20 wt% levels) and 2) pH of the PET NPs suspension (3, 4.5, and 6 levels) during the photocatalytic degradation of 100 mg/L of PET NPs using a 0.125 g/L catalyst loading. The response used to assess the degradation was the carbonyl index (FTIR analysis) at accumulated energy of 600 kJ/m^2 (**SI,** Table S1).

Under the optimized conditions for the photocatalytic degradation of PET NPs using TiO_2/MIL-100(Fe), the photolysis and photocatalysis over TiO_2 and TiO_2/MIL-100(Fe) in the presence of scavenger agents were performed. The reactive species responsible for the photocatalytic degradation of PET NPs were studied using t-butanol (t-BuOH) to inhibit HO• and 2-propanol (2-PrOH) to inhibit both HO• and h^+ employing a molar ratio of 1:100 (pollutant: scavenger agent) [33].

3. Results and discussion

3.1. Characterization of materials

The PET NPs produced from commercially available PET water

plastic bottles were characterized by SEM and FTIR spectroscopy (Fig. S1). The formation of spherical particle aggregates with homogeneous size distribution and an average size of 111 ± 51 nm was observed (Fig. S1a), classifying them as NPs (diameter < 1 μm) [3,5]. Aggregates of PET NPs have also been described in earlier studies [34,35]. The FTIR spectrum of the NPs (Fig. S1b) shows a symmetrical stretching band at 1718 cm^{-1} corresponding to the C═O bond, two stretching modes, a strong peak at 1255 cm^{-1} and a doublet at 1124 cm^{-1} for the C(=O)-O and C-O groups. The absorption band at 2960 cm^{-1} is assigned to the asymmetric stretching vibration of the C-H bond. The three stretching vibrations at 1020, 873, and 727 cm^{-1} are assigned to the out-of-plane vibrations of the C–H bond of the aromatic ring, while the stretch signal at 1506 cm^{-1} is assigned to the aromatic backbone stretching the C═C bond. The FTIR spectrum of PET NPs was consistent with those previously reported in the literature for PET [27,34,35].

Thermogravimetric analysis is an important tool for studying the thermal stability of MIL-100(Fe) metal-organic frameworks. Fig. S2 depicts the thermogram, which shows three stages of weight loss. The water and solvent being trapped in the pores of the MOF caused the first weight loss (approximately 20%) between 25 °C and 150 °C. The second loss (35%) occurred between 150 °C and 350 °C due to the removal of unbound linkers trapped in the porous material. In comparison, the third loss (~65%) occurred between 350 °C and 550 °C due to the framework decomposition and iron reduction. When the temperature was raised above 550 °C, the weight of MIL-100(Fe) barely changed, indicating that the organic ligands were pyrolyzed. This finding was similar to those in previous studies [20,36], the TiO_2/MIL-100(Fe) composites were therefore calcined at 350 °C.

The morphology of the prepared materials was observed by SEM analysis. The SEM image of MIL-100(Fe) is shown in Fig. 1a. The crystals did not show an octahedral shape [37], observing agglomerates of flaky-like particles, in agreement with a previous study [38]. The particle sizes range from 35 to 65 nm. The EDS measurements (Fig. 1d) revealed the presence of Fe, O, and C. The content estimated experimentally by EDS (25.51 wt% of Fe, 38.97 wt% of O, and 32.91 wt% of C) was comparable to the theoretical values for the condensed formula of the MOF ($Fe_3H_{17}O_{16}C_{18}$).

The SEM images of TiO_2 and TiO_2/MIL-100(Fe) 12.5 wt% composites are shown in Figs. 1b and 1c. The samples consisted of spherical nanoparticles that tend to agglomerate. The incorporation of MIL-100 (Fe) into the TiO_2 particles increased the particle size of TiO_2, observing a slightly smaller particle size in TiO_2 (29 ± 6 nm) than that in the TiO_2/MIL-100(Fe) 12.5 wt% composite (54 ± 15 nm). The signals corresponding to Ti, O, and Fe were observed in the EDS map of the TiO_2/MIL-100(Fe) 12.5 wt% composite (Fig. 1e). In contrast, Ti and O were observed in the TiO_2 sample (Fig. 1f). The semiquantitative analysis showed that incorporated iron from MIL-100(Fe) into the TiO_2/MIL-100(Fe) composite corresponded to 3.08 wt%, showing excellent agreement with the theoretical Fe content (3.19 wt%) [37,38].

The total Fe content in the composites was determined by AAS after the digestion of catalyst samples. Iron content was related to MIL-100 (Fe) incorporated into TiO_2. The obtained results were compared with the theoretical amount added during the synthesis (Table 1). The iron incorporated as MIL-100(Fe) was close to the theoretical value added with an error of less than 12%, demonstrating that the hydrothermal synthesis method can successfully incorporate MIL-100(Fe) into TiO_2.

The SEM/EDS further characterized the supported catalyst revealing that perlite mineral particles showed high porosity, which makes this material an effective support for TiO_2-based catalysts (Fig. S3a). The acidic dispersion of TiO_2/MIL-100(Fe) was deposited on the perlite mineral, forming a uniform perlite coating (Fig. S3b). The EDS spectrum of the perlite mineral grains showed the aluminosilicate structure composition (Fig. S3c) [31]. In contrast, the EDS pattern of perlite coated with TiO_2/MIL-100(Fe) (Fig. S3d) presented titanium (47.50 wt %), oxygen (14.28 wt%), iron (2.50 wt%) and a small amount of Si (0.28 wt%) from perlite. These results confirmed the deposition of the composite on perlite mineral grains.

The FTIR spectrum of MIL-100(Fe) (Fig. 2a) showed the bands at 3368 cm^{-1} for O-H bonds and at 1628 and 1376 cm^{-1} for the stretching modes of C═O and C-O bonds in the carboxylate group, respectively.

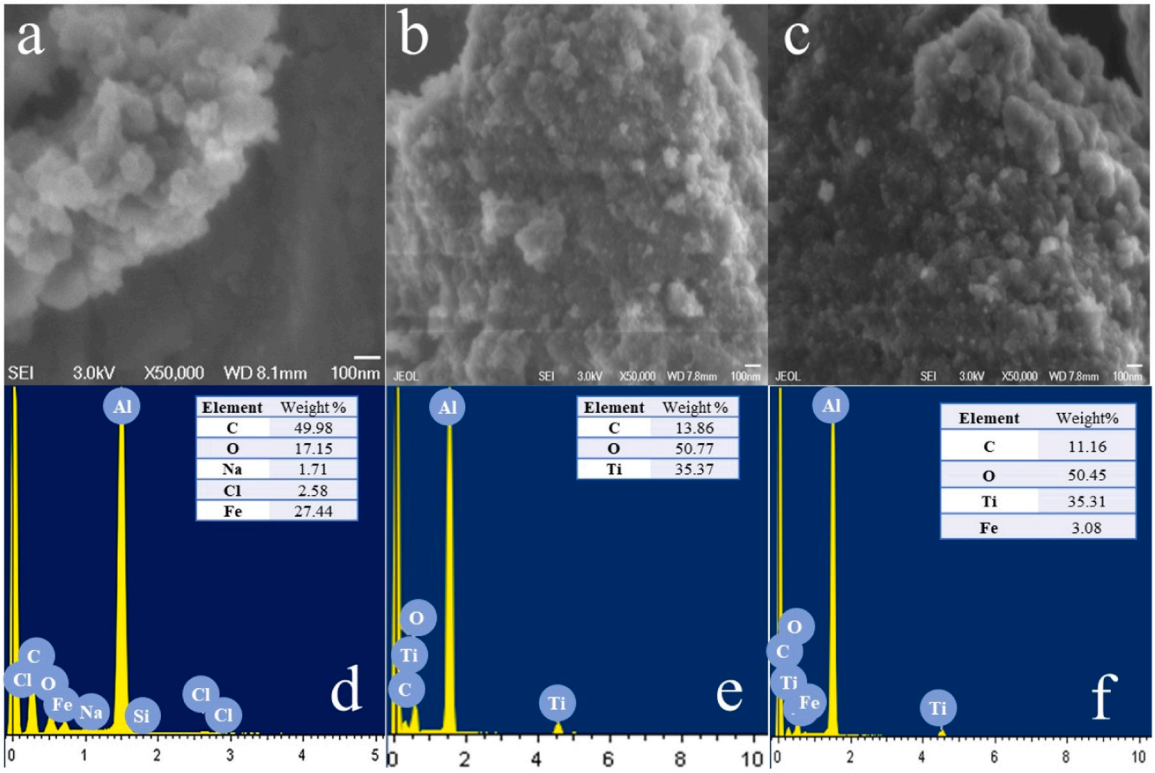

Fig. 1. SEM morphology and EDS spectra of a) and d) MIL-100(Fe), b) and e) TiO_2, and c) and f) TiO_2/MIL-100(Fe) 12.5 wt% samples.

Table 1
Summary of physicochemical characteristics of the prepared nanomaterials.

Material	Crystallite size (nm)[a]	E_g (eV)[b]	BET surface area (m^2/g)[c]	Average BJH pore size (nm)[c]	Average pore volume (cm^3/g)[c]	MIL-100(Fe) added (%)	MIL-100(Fe) incorporated (%)[d]
MIL-100(Fe)		1.93	732.1	4.02	0.74		
TiO_2	4.0	3.03	128.2	11.96	0.38		
TiO_2/MIL-100(Fe) 5%	3.9	2.65	174.4	9.23	0.40	5.00	4.40 ± 0.20
TiO_2/MIL-100(Fe) 12.5%	3.7	2.29	179.0	7.25	0.32	12.50	12.24 ± 0.40
TiO_2/MIL-100(Fe) 20%	3.0	2.21	198.8	8.38	0.42	20.00	19.15 ± 0.77

[a] XRD analysis (Scherrer equation)
[b] UV-Vis DRS analysis
[c] N_2 physisorption analysis
[d] Atomic Absorption Spectroscopy

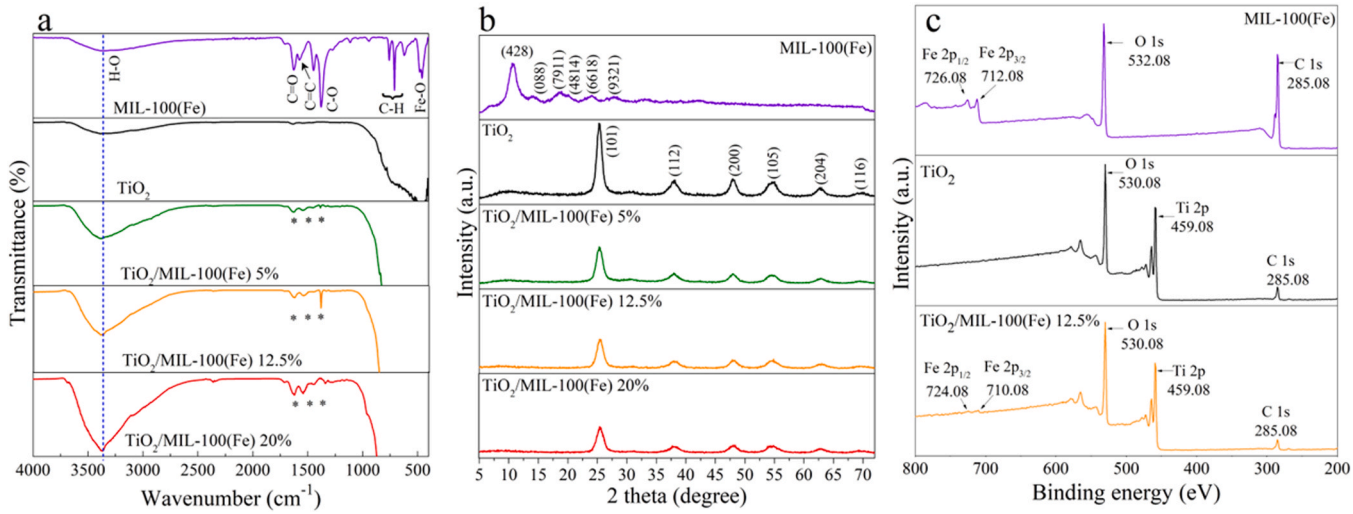

Fig. 2. a) FTIR spectra and b) powder X-ray diffraction (XRD) patterns of the as-prepared materials, and c) XPS survey spectra of MIL-100(Fe), TiO_2, and TiO_2/MIL-100(Fe).

Simultaneously, the signals for the C═C stretching mode at 1571 cm^{-1} and stretching out-of-the-plane C-H vibrations of the aromatic ring structure were found at 760, 710 and 622 cm^{-1}. The stretching vibration at 457 cm^{-1} corresponding to the distinctive Fe-O bond of the iron ion-coordinated carboxyl group in the MIL-100(Fe) structure was observed [37].

The FTIR spectrum of TiO_2 (Fig. 2a) showed peaks at 3410 cm^{-1} and 1656 cm^{-1} related to the O-H stretching and bending modes of the surface hydroxyl groups, respectively. The broad band at values below 900 cm^{-1} corresponded to the Ti-O-Ti stretching and bending modes. The peaks at 1620, 1540, and 1380 cm^{-1} assigned to the stretching modes of C═O, C═C (aromatic ring), and C-O were observed in the spectra of the TiO_2/MIL-100(Fe) composites, all of which were ascribed to MIL-100 (Fe). According to Hejazi et al., these findings could indicate the coexistence of MIL-100(Fe) and TiO_2 in these composite materials [20]. In addition, the O-H broadband increased in intensity as the MIL-100(Fe) loading grew in the TiO_2/MIL-100(Fe) catalysts. The surface hydroxyl groups are critical in the photocatalytic reaction because they interact with h^+ to promote the production of $^{\bullet}OH$ radicals that could enhance the photocatalytic performance of the prepared composites [39].

XRD was used to examine the crystalline structures of the catalysts (Fig. 2b). The XRD diffractogram of MIL-100(Fe) revealed characteristic peaks at 10.56°, 14.15°, 18.95°, 20.16°, 24.06° and 27.60° associated with crystalline MIL-100(Fe) [20,37]. The TiO_2/MIL-100(Fe) samples showed the diffraction peaks assigned to planes (101), (112), (200), (105), (204), (116), and (215) of TiO_2 anatase crystalline phase (JCPDS No. 21–1272) [40]. No additional diffraction peaks related to the MIL-100(Fe) crystalline phase were identified when MIL-100(Fe) was incorporated into the TiO_2. This result can be attributed to the low crystallinity of MIL-100(Fe) [23]. However, the incorporation of MIL-100(Fe) into TiO_2 decreased its crystallinity of TiO_2 [23]. Table 1 shows the physicochemical characteristics of the prepared materials where it can be seen that TiO_2 crystallite size slightly decreased from 4.0 to 3.0 nm when the amount of MIL-100(Fe) incorporated into the composites increased.

X-ray photoelectron spectroscopy (XPS) was used to analyze the elemental composition and electronic and chemical states of the elements in MIL-100(Fe), TiO_2, and TiO_2/MIL-100(Fe). The survey XPS spectrum of MIL-100(Fe) (Fig. 2c) shows clear peaks for the C, O, and Fe elements. Carbon could be present due to surface adventitious carbon from contamination and for the MOF composition. The TiO_2 spectrum contains C, Ti, and O elements, whereas Fe from the organic moiety was found in the TiO_2/MIL-100(Fe) 12.5% composite in addition to Ti, C, and O. Fig. 3 depicts high-resolution spectra of Ti 2p, O 1 s and Fe 2p. The Ti 2p high-resolution spectra of TiO_2 and TiO_2/MIL-100(Fe) exhibit two peaks at 464.08 eV and 458.47 eV, corresponding to the Ti 2p½ and Ti $2p_{3/2}$ binding energies associated with the Ti^{4+} valence state in anatase TiO_2 (Fig. 3a). Although the Ti 2p½ and Ti $2p_{3/2}$ peaks in TiO_2/MIL-100(Fe) are consistent with the characteristic states of Ti in bare TiO_2 [23,41], the Ti $2p_{3/2}$ peak for TiO_2/MIL-100(Fe) is deconvoluted into two components at 459.38 and 458.45 eV, showing that the

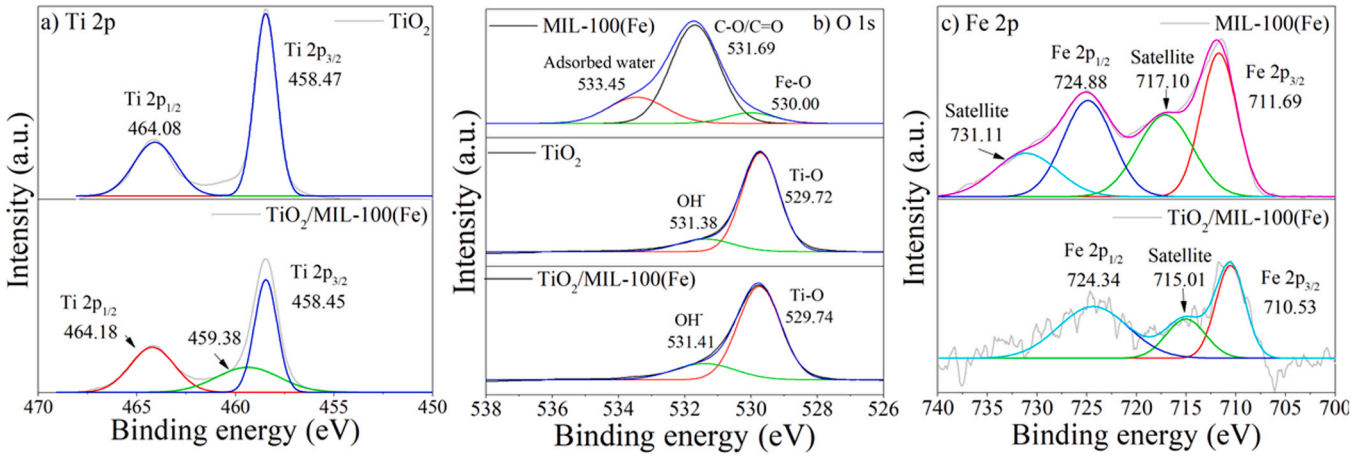

Fig. 3. High-resolution spectra of a) Ti 2p, b) O 1 s, and c) Fe 2p of MIL-100(Fe), TiO_2 and TiO_2/MIL-100(Fe) materials.

presence of Fe-O-Ti bonds creates two types of electronic environments for Ti cations [19,42]. The deconvoluted O 1 s core level spectra are shown in Fig. 3b. The spectrum of the MIL-100(Fe) sample was deconvoluted into three peaks centered at 530.00, 531.69, and 533.45 eV, representing Fe-O species in the crystal lattice, C–O/C═O bonds, and adsorbed water or hydroxyl groups, respectively [41]. The O 1 s spectrum of TiO_2 is conformed by two peaks located at 529.72 eV and 531.38 eV, which belong to Ti-O bonds and surface hydroxyl groups (OH-), respectively. In the composite, the O 1 s spectrum showed two signals, the peak at the binding energies of 529.74 eV is related to Fe-O, and the Ti-O bonds are due to overlapping in the O 1 s XPS spectrum, while the peak at 531.41 eV is related to the organic linker Fe-O-C species present in the intrinsic structure of MIL-100(Fe) [19,23,41].

The Fe 2p core spectra of MIL-100(Fe) and TiO_2/MIL-100(Fe)

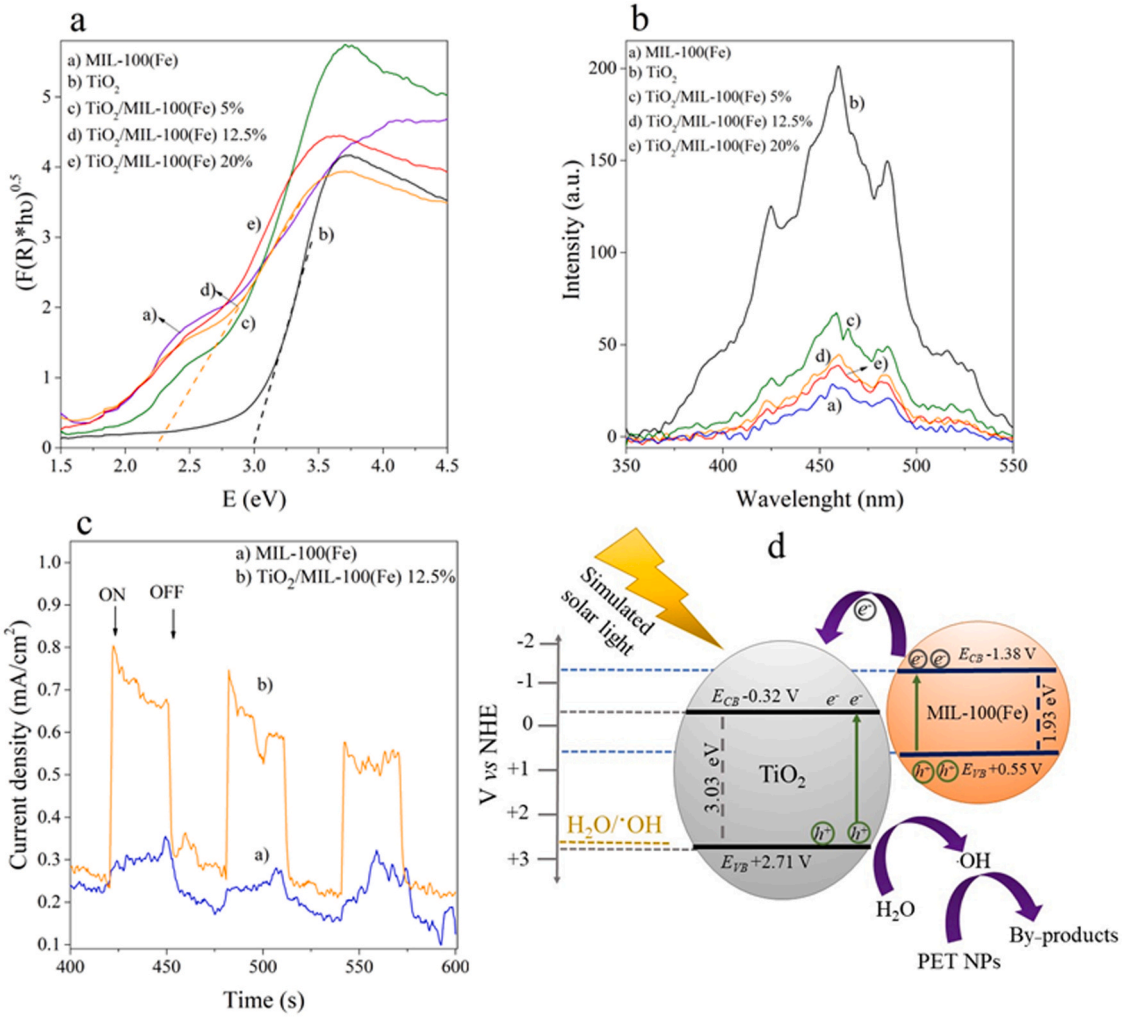

Fig. 4. a) Tauc plots, b) PL spectra, and c) photocurrent response of the prepared materials, and d) proposed photocatalytic mechanism.

composite are shown in Fig. 3c. For the MIL-100(Fe) material, the spectrum is deconvoluted into two peaks at 724.88 eV and 711.69 eV associated with Fe $2p_{1/2}$ and Fe $2p_{3/2}$, respectively, and two satellite peaks of Fe 2p1/2 and Fe 2p3/2 at 731.11 and 717.10 eV, respectively. The satellite peak at 717.10 eV corresponds to Fe(III) in MIL-100(Fe) [43]. Notably, the peaks in TiO_2/MIL-100(Fe) show a negative shift when compared to pristine MIL-100(Fe) due to the formation of Fe-O-Ti-bonding in the TiO_2 lattice [36].

The textural features of the synthesized materials were examined by N_2 physisorption analysis (Fig. S4) and categorized according to the IUPAC classification [44]. MIL-100(Fe) demonstrated the coexistence of type I and type IV isotherms and a narrow type H1 hysteresis loop between 0.05 and 0.98 P/P_0 (Fig. S4a). According to the classification, the sample is a porous material with micropores and mesopores. The isotherms of TiO_2 and TiO_2/MIL-100(Fe) composites are categorized as type IV by IUPAC, with an H2 hysteresis loop at 0.60–0.99 P/P_0, corresponding to capillary condensation occurring in the mesoporous structure. The pore size distribution of MIL-100(Fe) with average pore sizes of 4.02 nm, classifying it as a mesoporous material, is shown in Fig. S4b. Table 1 shows the specific surface area, pore volume, and pore size of the materials. The BET surface area of MIL-100(Fe) was 732.1 m^2/g, and the pore volume was 0.74 cm^3/g. As expected, as the MIL-100(Fe) loading increased in the TiO_2/MIL-100(Fe) composites, the BET surface area increased from 128.2 m^2/g in TiO_2 to 198.8 m^2/g in TiO_2/MIL-100(Fe) 20%. The average pore size increased from 4.02 nm in MIL-100(Fe) to 8.38 nm in TiO_2/MIL-100(Fe) 20 wt% while the pore volume decreased from 0.74 to 0.42 cm^3/g, indicating that MOF could cover the available TiO_2 pores. These findings were similar to those previously reported by Hejazi et al. [20].

The band gap energy values of the prepared materials related to the direct allowed transitions were estimated from the Tauc plots as shown in Fig. 4a. The MIL-100(Fe) incorporated into TiO_2 shifted the absorption edge of TiO_2 toward lower energy values, indicating that the composite exhibits strong absorption in the visible region. The composites exhibited reduced Eg values (2.21–2.65 eV) compared to TiO_2 (≈3.03 eV) (Table 1). Additionally, the TiO_2/MIL-100(Fe) composites showed a second band gap value consistent with that of MIL-100(Fe) (1.93 eV) that is characteristic of the 3d-3d transition of octahedral FeIIIO6 in MIL-100(Fe) [20,22]. According to Chen et al. [40], these data demonstrated the coupling of MIL-100(Fe) with TiO_2. As a result, the MIL-100(Fe) loading narrows the band gap of TiO_2 and enhances the visible light absorption capacity, improving the use of visible light during the photocatalytic process. The photoluminescence spectra of the materials were obtained to further study the separation of photogenerated e^-/h^+ pairs (Fig. 4b). The broad signal corresponding to the 375–500 nm region with a maximum at 460 nm was attributed to self-trapped e^- and h^+ radiative recombination [45]. A decrease in the photoluminescence intensity is related to a decrease in the recombination rate between photogenerated e^- and h^+, and hence, an increase in photocatalytic activity [46]. The PL emission peaks intensity of the synthesized samples decreases in the order of TiO_2 > TiO_2/MIL-100(Fe) 5 wt% > TiO_2/MIL-100(Fe) 12.5 wt% > TiO_2/MIL-100(Fe) 20 wt% > MIL-100(Fe), showing that their photocatalytic performance can be enhanced in the same order.

The photoexcited charge separation capabilities of the synthesized materials were evaluated by photocurrent measurements. The photocurrent density of the catalyst-coated working electrode during three on-off cycles under simulated sunlight is shown in Fig. 4c. The photocurrent density of TiO_2/MIL-100(Fe) 12.5 wt% was higher than that of pure MIL-100(Fe); thus, the incorporation of MIL-100(Fe) into TiO_2 efficiently promoted the separation of e^- and h^+, which is beneficial to TiO_2/MIL-100(Fe) 12.5 wt% charge transfer process. The improved charge carriers separation at the TiO_2/MIL-100(Fe) 12.5 wt% composite is expected to improve the photocatalytic response during the PET NPs degradation [47].

The Mott-Schottky analysis was carried out, and the resulting plots are shown in Fig. S5. The positive slope of the Mott-Schottky curves demonstrated the n-type semiconductor characteristics of TiO_2 and MIL-100(Fe). The flat band potentials of MIL-100(Fe) and TiO_2 were calculated using Mott-Schottky plots and estimated to be − 1.78 and − 0.72 V vs Ag/AgCl, corresponding to potentials of - 1.58 and - 0.52 V vs *NHE*, respectively. The conduction band (CB) potentials of MIL-100(Fe) and TiO_2 were -1.38 and -0.32 V, vs *NHE*. The valence band (VB) potentials were determined to be + 0.55 V and + 2.71 V vs NHE, respectively, based on the band gap energy values calculated from the DRS-UV-Vis spectra of MIL-100(Fe) and TiO_2 [48]. Given the suitable CB of TiO_2 and MIL-100(Fe), it is hypothesized that under simulated sunlight, e^- may migrate from the CB of MIL-100(Fe) to that of TiO_2. At the same time, photogenerated h^+ are transported from the VB of TiO_2 to that of MIL-100(Fe) through the interaction between MIL-100(Fe) and TiO_2. Thus, the charge transfer between TiO_2 and MIL-100(Fe) resulted in charge separation by decreasing the e^-/h^+ recombination and increasing the photocatalytic efficiency to degrade PET NPs. These findings were linked to the photocurrent and photoluminescence data. Based on these results, the possible charge separation mechanism of the TiO_2/MIL-100(Fe) composite was proposed in the scheme shown in Fig. 4d.

3.2. Photocatalytic activity evaluation

The effect of the factors 1) incorporated content of MIL-100(Fe) into the TiO_2 photocatalyst (5, 12.5, and 20 wt%) and 2) pH of the NPs suspension (3, 4.5, and 6) during the photocatalytic degradation of PET NPs under simulated solar light was statistically analyzed using ANOVA with a 95% confidence interval at a significance level of $p < 0.05$ (Table S2). The oxidation of PET NPs was evaluated by changes in carbonyl index (CI) measured by FTIR [49]. The supplementary information (SI) described the statistical analysis of the results showing the graphical representation of the factors in 3D response surface and 2D contour plots (Fig. S6).

The influence of the initial pH value of the PET nanoplastics suspension showed that the photocatalytic degradation of NPs was higher in the acidic media (pH = 3) than in the near-neutral solution pH (pH = 6.0). Similarly, faster photocatalytic degradation of various polymers such as polymethylmethacrylate nanobeads (average size 105 nm) [10], HDPE-MPs (200–250 μm) [11], and HDPE-MPs (725 ± 108 μm) [50] was carried out in acidic pH media. The results were related to the Coulomb attraction between the plastic polymers and the catalyst surface that is favored under acidic media [10,11,50]. In contrast, Zhou et al. reported that the photocatalytic degradation of fiber-based PET MPs was favored in alkaline media due to the hydrolysis of PET-FMPs, which contributes to the high degradation efficiency [14]. PET is a polymer that does not readily degrade due to its aromatic groups, as suggested by the proposed mechanism described in previous studies (Equations S1-S6) [50,51].

Surface holes (h^+) can react with H_2O to produce $^{\bullet}OH$, which starts the degradation of the CH_2 group adjacent to the ester bond, resulting in the formation of an alkyl radical [R-CO•$CHCH_2O$-] (Eq. S1). This alkyl radical then reacts with oxygen to generate a peroxyl radical [R-CHOO•CH_2O-]n (Eq. S2), which takes hydrogen from other polymer chains to produce the hydroperoxide species [R-CHOOH-CH_2O-]n (Eq. S3), that is photolytically unstable [50]. As a result, the O-O bond of the hydroperoxide group is broken, resulting in free oxy radicals [R-CHO•CH_2O-]n and hydroxyl radicals ($^{\bullet}OH$) (Eq. S4). The free oxy radicals are reactive species capable of abstracting labile hydrogens from other polymer chains, resulting in photoproducts (Eq. S5) [50,51]. Excess of [H^+] in acidic media enhanced the NPs PET degradation by generating hydroperoxide species ([R-CHOOH-CH_2O-]n, Eq. S6), a key intermediate in the formation of oxy radicals [51].

The amount of MIL-100(Fe) incorporated into TiO_2, on the other hand, exhibited a slight curvature at the central point of the evaluated levels, showing the TiO_2/MIL-100(Fe) 12.5 wt% material a slightly better photocatalytic activity in the PET NPs degradation. The

interaction between TiO_2 and MIL-100(Fe) in the composite effectively separates the e^-/h^+ pairs. However, the amount of Fe-based MOF loaded into TiO_2 and the synthesis method used to prepare the composite may modify the alignment of the bands, impacting on the recombination rate of e^-/h^+ pairs and the photocatalytic performance of the material [19,46]. He et al. found that the TiO_2 P25/MIL-100(Fe) 19.4 wt% photocatalyst improved the tetracycline oxidation and Cr(VI) reduction over bare TiO_2 P25. The composite was prepared by growing MIL-100(Fe) crystals on TiO_2 using surface-coated FeOOH as a precursor [19]. Hierarchical sandwich-like TiO_2/MIL-100(Fe) synthesized by the self-assembly method with the addition of 33 wt% MIL-100(Fe) showed enhanced photocatalytic activity in the methylene blue decolorization compared with MIL-100(Fe) and TiO_2 [46].

The optimum process conditions were determined using the response surface methodology and desirability function with an initial pH of the NPs PET suspension of 3 and 12.5 wt% MIL-100 (Fe) incorporated in TiO_2 corresponds to a desired value of 0.7408. The predicted and experimental values for the carbonyl index were 0.978 and 0.994, respectively, indicating good agreement between the experimental data and quadratic model prediction. Control experiments using 12.5 wt% of MIL-100(Fe) in TiO_2 at an initial pH of 3 showed that the TiO_2/MIL-100 (Fe) 12.5 wt% material was more effective in degrading the PET NPs suspension under simulated solar light. This result is confirmed by an increase in the carbonyl index (CI = 0.99), a reduction in the turbidity ratio of the medium (0.454), and an increase in the content of TOC released (3.00 mg/L) (Fig. 5). In contrast, PET NPs were slowly degraded by direct photolysis (CI = 0.82, turbidity ratio = 0.849, released TOC = 1.73 mg/L) and by TiO_2-based photocatalysis (CI = 0.96, turbidity ratio = 0.539, released TOC = 2.12 mg/L).

An increase in the carbonyl index has been reported as a sign of polymer oxidation [49]. Furthermore, significant changes in the infrared spectrum were observed during PET degradation by photolysis and photocatalysis, which can be divided into three regions of the spectra (details in SI, Fig. S7) [52–54]. Vibrations in the C-H region (3000–2800 cm^{-1}, Fig. S7a), where the signal intensities at 2960 cm^{-1}, 2880 cm^{-1}, and 2853 cm^{-1} associated with symmetric and asymmetric C-H and -CH_2- bonds, decreased and almost disappeared during photolysis and heterogeneous photocatalysis [10]. The region of carbonyl vibrations of esters (C═O bond, 1714 cm^{-1}) (Fig. S7b) was significantly reduced with a shoulder at a shorter wavelength of 1685 cm^{-1}, due to the formation of terephthalic acid monomer, which produced a fragmentation of the polymer into monomeric units [10,11]. The region of 1350–950 cm^{-1} assigned to the C-O band of the ester group is shown in Fig. S7c. The spectra showed an increase in the intensity of the 1096 cm^{-1} band and a decrease in the signal at 1283 cm^{-1} attributed to ester stretching and IR vibrations of the ethylene glycol group, respectively, that were related to the photo-oxidation of PET.

Similarly, the decrease in the band intensity at 1340 cm^{-1} corresponds to the CH_2 wagging modes, which are converted into aldehyde end groups in the presence of reactive species. After irradiation, a reduction in the peak intensity at 970 cm^{-1} was observed, which was attributed to the C-H stretching of the ethylene glycol moiety. The decrease in this peak is related to the cleavage of ester linkages in the polymer chain during PET degradation [11,12]. Photocatalytic degradation of plastics is relatively recent, and few studies have reported the intermediates generated during PET oxidation. Zhou et al. evidenced the degradation of PET fiber-based microplastic by the average molecular weight reduction using a Bi_2O_3@N-TiO_2 heterojunction [14] and N-doped TiO_2 nanoflowers decorated with Pt nanoparticles [15]. Some of the identified intermediates in the filtrate by CG-MS were short-chain substances such as alcohols, carboxylic acids, aldehydes, esters, and olefins. The authors mentioned that identifying by-products during PET microplastic degradation is challenging due to the presence of multiple side reactions of intermediate products and the lack of in-situ characterization tests. To verify the photocatalytic degradation of PET NPs on 12.5 wt% TiO_2/MIL-100(Fe) material, SEM analysis was utilized. Fig. 6 displays SEM micrographs before and after 600 kJ/m^2 of UV accumulated energy. The microstructure surface of the PET NPs underwent noticeable changes, resulting in the formation of cavities due to photocatalytic oxidation reaction. These cavities could be generated due to volatile products that evolved from the degrading polymer NPs [55].

3.3. Identification of the reactive species by trapping experiments

The role of the superoxide ion radical $O_2^{\bullet-}$ in the photocatalytic degradation of PET NPs was not investigated because $HO_2\bullet$ is the dominant species at pH 3 (pKa = 4.8) [33]. On the other hand, the photocatalytic degradation of PET NPs decreased rapidly after the addition of the $^{\bullet}OH$ scavenger (t-BuOH), as indicated by the increase in the C═O bond signal intensity (1714 cm^{-1}) as shown in the FT-IR spectrum (Fig. S8a). On the other hand, no difference in the FTIR signal intensity was observed with the addition of 2-PrOH and t-BuOH. The CI calculated from the FTIR spectra (Fig. S8a) confirmed the role of scavengers in plastic degradation. As shown in Table S3, the initial PET NPs suspension has a CI value of 0.62. PET NPs degradation increased the CI to 0.99 during the photocatalytic degradation without scavenger.

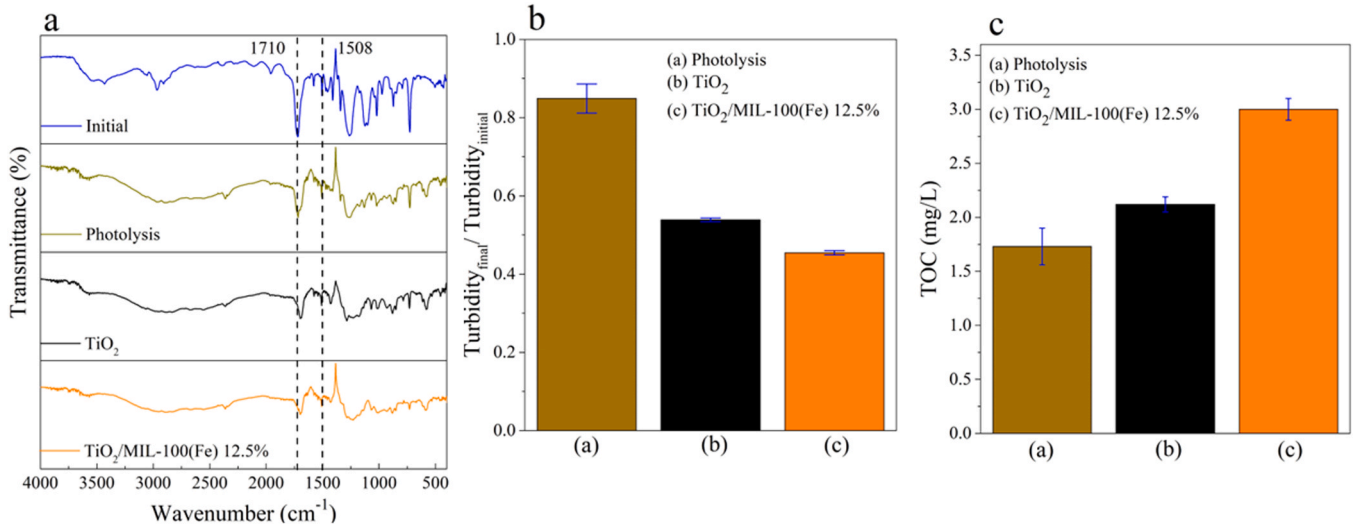

Fig. 5. a) FTIR of PET NPs before and after degradation with 600 kJ/m^2 of UV accumulated energy (a), b) change in turbidity media at 620 nm (n = 3 replicates), and c) released TOC content in solution during photocatalysis and photolysis of PET NPs (n = 3 replicates).

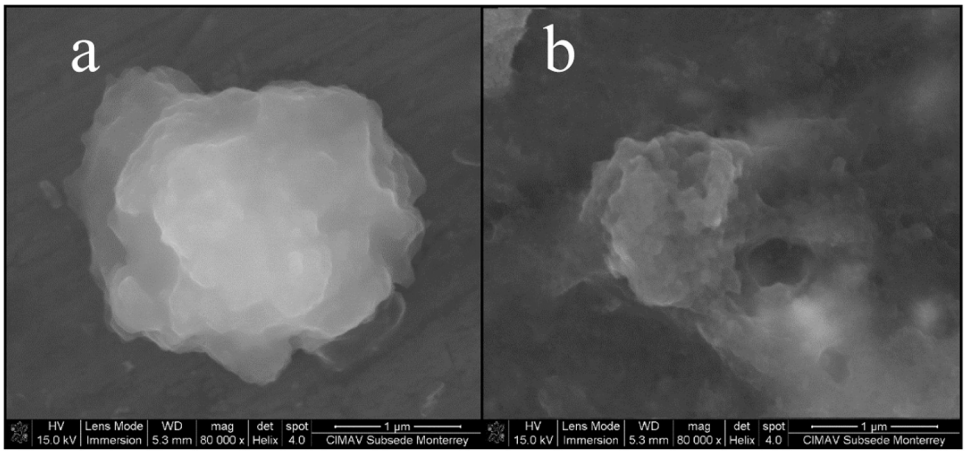

Fig. 6. SEM images of PET NPs a) before and b) after photocatalytic degradation with 600 kJ/m^2 of UV accumulated energy on 12.5 wt% TiO_2/MIL-100 (Fe) material.

The CI values of PET NPs degraded by photocatalysis in the presence of t-BuOH and 2-PrOH scavengers showed CI values of 0.77 and 0.78, respectively, proving that h^+ and $^\bullet$OH radicals are the reactive species involved in the photocatalytic degradation of PET polymer matrix by the TiO_2/MIL-100(Fe) composite under simulated sunlight. Turbidity measurements (Fig. S8b and Table S4) also confirmed these findings with similar inhibition of the response during the photocatalytic process using 2-PrOH and t-BuOH scavengers. These results were supported by Mott-Schottky analysis (Section 3.2). The photogenerated h^+ in the VB of MIL-100(Fe) oxidize PET NPs or react with H_2O to form $^\bullet$OH radicals as in the proposed schematic mechanism depicted in Fig. 4d. However, since the calculated VB potential of MIL-100(Fe) was less positive than the standard redox potential of $^\bullet OH/H_2O$ (2.68 eV vs *NHE*), it could imply that the photogenerated h^+ cannot oxidize H_2O to $^\bullet$OH radicals. Thus, the $^\bullet$OH radicals could be produced at the higher positive VB of TiO_2 in the TiO_2/MIL-100(Fe) composite to further contribute to the degradation of PET NPs.

It has been described that the main reaction pathway during the photocatalytic degradation of polymers such as HDPE MP by BiOCl catalysts [11] and C, N-TiO_2 powders [50] was through the formation of $^\bullet$OH radicals. On the other hand, $O_2^{\bullet-}$, singlet oxygen, and h^+ were the active species involved in the oxidation of fiber-based microplastic of PET using N-doped TiO_2 nanoflowers decorated with Pt nanoparticles [15].

4. Conclusions

MIL-100(Fe) coupled with TiO_2 semiconductor was prepared using a simple microwave/solvothermal procedure followed by a post-annealing approach. The resultant material showed better photocatalytic performance than pure TiO_2 for PET NPs degradation. The TiO_2/MIL-100(Fe) catalyst presented the anatase crystalline phase of TiO_2 under simulated solar light. The improved photocatalytic activity of TiO_2/MIL-100(Fe) was ascribed to the higher surface area, extended absorption in the visible light region, and lower Eg than that of TiO_2. MIL-100(Fe) and TiO_2 interaction also favored effective e^-/h^+ separation. The optimum conditions for the heterogeneous photocatalytic degradation of PET NPs were at acidic pH (pH=3) using the composite of 12.5 wt% MIL-100(Fe) incorporated into TiO_2. The scavenger experiments revealed that the reactive species $^\bullet$OH and h^+ were involved in the degradation of PET NPs. For the first time, it was demonstrated that the photocatalytic process using TiO_2/MIL-100(Fe) under simulated sunlight is an alternative method for degrading PET NPs, a resistant synthetic plastic polymer, providing the basis for future research focusing on the degradation mechanism of PET NPs.

CRediT authorship contribution statement

César A. Rojas-Guerrero: Methodology, investigation, formal analysis, writing – original draft. Minerva Villanueva-Rodríguez: Supervision, writing – review & editing. Jorge Luis Guzmán-Mar: Formal analysis, validation, writing – review & editing. Aracely Hernández-Ramírez: Formal analysis, writing – review & editing. Erika. I. Cedillo-González: Conceptualization, writing – review & editing. Francisco E. Longoria Rodríguez: Formal analysis, validation, visualization. Laura Hinojosa-Reyes: Conceptualization, supervision, funding acquisition, writing – review & editing.

Declaration of Competing Interest

The authors declare that they have no known competing financial interests or personal relationships that could have appeared to influence the work reported in this paper.

Data availability

Data will be made available on request.

Acknowledgment

This work was supported by Facultad de Ciencias Químicas and CONAHCYT (Ciencia de Frontera 2019, Project No. 1727980). C.A. Rojas-Guerrero thanks CONAHCYT for the scholarship (Grant No. 1080939). The authors gratefully acknowledge Dr. D. Pino-Sandoval for the technical assistance in performing electrochemical measurements.

Appendix A. Supporting information

Supplementary data associated with this article can be found in the online version at doi:10.1016/j.jece.2023.110415.

References

[1] M.R. Karimi-Estahbanati, M. Kiendrebeogo, A. Khosravanipour-Mostafazadeh, P. Drogui, R.D. Tyagi, Treatment processes for microplastics and nanoplastics in waters: State-of-the-art review, Mar. Pollut. Bull. 168 (2021), 112374, https://doi.org/10.1016/j.marpolbul.2021.112374.
[2] F. Lionetto, C. Esposito-Corcione, An overview of the sorption studies of contaminants on poly(ethylene terephthalate) microplastics in the marine environment, J. Mar. Sci. Eng. 9 (2021) 445, https://doi.org/10.3390/jmse9040445.
[3] P. Li, Q. Li, Z. Hao, S. Yu, J. Liu, Analytical methods and environmental processes of nanoplastics, J. Environ. Sci. 94 (2020) 88–99, https://doi.org/10.1016/j.jes.2020.03.057.

[4] M. Djapovic, D. Milivojevic, T. Ilic-Tomic, M. Ljesevic, E. Nikolaivits, E. Topakas, V. Maslak, J. Nikodinovic-Runic, Synthesis and characterization of polyethylene terephthalate (PET) precursors and potential degradation products: Toxicity study and application in discovery of novel PETases, Chemosphere 275 (2021), 130005, https://doi.org/10.1016/j.chemosphere.2021.130005.

[5] M. Shen, Y. Zhang, Y. Zhu, B. Song, G. Zeng, D. Hu, X. Wen, X. Ren, Recent advances in toxicological research of nanoplastics in the environment: A review, Environ. Pollut. 252 (2019) 511–521, https://doi.org/10.1016/j.envpol.2019.05.102.

[6] I. Nabi, A.U.R. Bacha, F. Ahmad, L. Zhang, Application of titanium dioxide for the photocatalytic degradation of macro- and micro-plastics: A review, J. Environ. Chem. Eng. 9 (2021), 105964, https://doi.org/10.1016/j.jece.2021.105964.

[7] H.K. Paumo, S. Dalhatou, L.M. Katata-Seru, B.P. Kamdem, J.O. Tijani, V. Vishwanathan, A. Kane, I. Bahadur, TiO_2 assisted photocatalysts for degradation of emerging organic pollutants in water and wastewater, J. Mol. Liq. 331 (2021), 115458, https://doi.org/10.1016/j.molliq.2021.115458.

[8] Z. Chen, X. Liu, W. Wei, H. Chen, B.J. Ni, Removal of microplastics and nanoplastics from urban waters: Separation and degradation, Water Res 221 (2022) (2022), 118820, https://doi.org/10.1016/j.watres.2022.1188208.

[9] A. Bianco, F. Sordello, M. Ehn, D. Vione, M. Passananti, Degradation of nanoplastics in the environment: Reactivity and impact on atmospheric and surface waters, Sci. Total Environ. 742 (2020), 140413, https://doi.org/10.1016/j.scitotenv.2020.140413.

[10] P.H. Allé, P. Garcia-Muñoz, K. Adouby, N. Keller, D. Robert, Efficient photocatalytic mineralization of polymethylmethacrylate and polystyrene nanoplastics by TiO_2/β-SiC alveolar foams, Environ. Chem. Lett. 19 (2020) 1803–1808, https://doi.org/10.1007/s10311-020-01099-2.

[11] R. Jiang, G. Lu, Z. Yan, J. Liu, D. Wu, Y. Wang, Microplastic degradation by hydroxy-rich bismuth oxychloride, J. Hazard. Mater. 405 (2021), 124247, https://doi.org/10.1016/j.jhazmat.2020.124247.

[12] L.P. Domínguez-Jaimes, E.I. Cedillo-González, E. Luevano-Hipolito, J.D. Acuña-Bedoya, J.M. Hernández-López, Degradation of primary nanoplastics by photocatalysis using different anodized TiO_2 structures, J. Hazard. Mater. 413 (2021), 125452, https://doi.org/10.1016/j.jhazmat.2021.125452.

[13] J.D. Acuña-Bedoya, E. Luévano-Hipólito, E.I. Cedillo-González, L.P. Domínguez-Jaimes, A.M. Hurtado, J.M. Hernández-López, Boosting visible-light photocatalytic degradation of polystyrene nanoplastics with immobilized CuxO obtained by anodization, J. Environ. Chem. Eng. 9 (2021), 106208, https://doi.org/10.1016/j.jece.2021.106208.

[14] D. Zhou, L. Wang, F. Zhang, J. Wu, H. Wang, J. Yang, J. Feasible, Degradation of polyethylene terephthalate fiber-based microplastics in alkaline media with Bi_2O_3@N-TiO_2 Z-scheme photocatalytic system, Adv. Sustain. Syst. 6 (2022) 2100516, https://doi.org/10.1002/adsu.202100516.

[15] D. Zhou, H. Luo, F. Zhang, J. Wu, J. Yang, H. Wang, Efficient photocatalytic degradation of the persistent PET fiber-based microplastics over Pt nanoparticles decorated N-doped TiO_2 nanoflowers, Adv. Fiber Mater. 4 (2022) 1094–1107, https://doi.org/10.1007/s42765-022-00149-4.

[16] V. García-Salcido, P. Mercado-Oliva, J.L. Guzmán-Mar, B.I. Kharisov, L. Hinojosa-Reyes, MOF-based composites for visible-light-driven heterogeneous photocatalysis: Synthesis, characterization and environmental application studies, J. Solid State Chem. 307 (2022), 122801, https://doi.org/10.1016/j.jssc.2021.122801.

[17] Q. Wang, Q. Gao, A.M. Al-Enizi, A. Nafady, S. Ma, Recent advances in MOF-based photocatalysis: environmental remediation under visible light, Inorg. Chem. Front. 7 (2020) 300–339, https://doi.org/10.1039/C9QI01120J.

[18] S. Gautam, H. Agrawal, M. Thakur, A. Akbari, H. Sharda, R. Kaur, M. Amini, Metal oxides and metal organic frameworks for the photocatalytic degradation: A review, J. Environ. Chem. Eng. 8 (2020), 103726, https://doi.org/10.1016/j.jece.2020.103726.

[19] X. He, H. Fang, D.J. Gosztola, Z. Jiang, P. Jena, W.N. Wang, Mechanistic insight into photocatalytic pathways of MIL-100(Fe)/TiO_2 composites, ACS Appl. Mater. Interfaces 11 (2019) 12516–12524, https://doi.org/10.1021/acsami.9b00223.

[20] R. Hejazi, A.R. Mahjoub, A.H.C. Khavar, Z. Khazaee, Fabrication of novel type visible-light-driven TiO_2@MIL-100 (Fe) microspheres with high photocatalytic performance for removal of organic pollutants, J. Photochem. Photobiol. A Chem. 400 (2020), 112644, https://doi.org/10.1016/j.jphotochem.2020.112644.

[21] L. Chen, X. Wang, Z. Rao, Z. Tang, Y. Wang, G. Shi, G. Lu, X. Xie, D. Chen, J. Sun, In-situ synthesis of Z-scheme MIL-100(Fe)/α-Fe_2O_3 heterojunction for enhanced adsorption and visible-light photocatalytic oxidation of O-xylene, Chem. Eng. J. 416 (2021), 129112, https://doi.org/10.1016/j.cej.2021.129112.

[22] J. Huang, H. Song, C. Chen, Y. Yang, N. Xu, X. Ji, C. Li, J.-A. You, Facile synthesis of N-doped TiO_2 nanoparticles caged in MIL-100(Fe) for photocatalytic degradation of organic dyes under visible light irradiation, J. Environ. Chem. Eng. 5 (2017) 2579–2585, https://doi.org/10.1016/j.jece.2017.05.012.

[23] L. Liu, Y. Liu, X. Wang, N. Hu, Y. Li, C. Li, Y. Meng, Y. An, Synergistic effect of B-TiO_2 and MIL-100(Fe) for high-efficiency photocatalysis in methylene blue degradation, Appl. Surf. Sci. 561 (2021), 149969, https://doi.org/10.1016/j.apsusc.2021.149969.

[24] M.C. Ariza-Tarazona, J.F. Villarreal-Chiu, V. Barbieri, C. Siligardi, E.I. Cedillo-González, New strategy for microplastic degradation: Green photocatalysis using a protein-based porous N-TiO_2 semiconductor, Ceram. Int. 45 (2019) 9618–9624, https://doi.org/10.1016/j.ceramint.2018.10.208.

[25] T.S. Tofa, K.L. Kunjali, S. Paul, J. Dutta, Visible light photocatalytic degradation of microplastic residues with zinc oxide nanorods, Environ. Chem. Lett. 17 (2019) 1341–1346, https://doi.org/10.1007/s10311-019-00859-z.

[26] Z. Xing, J. Zhang, J. Cui, J. Yin, T. Zhao, J. Kuang, Z. Xiu, N. Wan, W. Zhou, Recent advances in floating TiO_2-based photocatalysts for environmental application, Appl. Catal. B Environ. 225 (2018) 452–467, https://doi.org/10.1016/j.apcatb.2017.12.005.

[27] A.G. Rodríguez-Hernández, J.A. Muñoz-Tabares, J.C. Aguilar-Guzmán, R. Vázquez-Duhalt, A novel and simple method for polyethylene terephthalate (PET) nanoparticle production, Environ. Sci. Nano 6 (2019) 2031–2036, https://doi.org/10.1039/C9EN00365G.

[28] K. Guesh, C.A.D. Caiuby, Á. Mayoral, M. Díaz-García, I. Díaz, M. Sánchez-Sánchez, Sustainable preparation of MIL-100(Fe) and its photocatalytic behaviour in the degradation of methyl orange in water, Cryst. Growth Des. 17 (2017) 1806–1813, https://doi.org/10.1021/acs.cgd.6b01776.

[29] L. Cano-Casanova, A. Amorós-Pérez, M. Ouzzine, M.A. Lillo-Ródenas, M.C. Román-Martínez, One step hydrothermal synthesis of TiO_2 with variable HCl concentration: Detailed characterization and photocatalytic activity in propene oxidation, Appl. Catal. B Environ. 220 (2018) 645–653, https://doi.org/10.1016/j.apcatb.2017.08.060.

[30] S.N. Hosseini, S.M. Borghei, M. Vossoughi, N. Taghavinia, Immobilization of TiO_2 on perlite granules for photocatalytic degradation of phenol, Appl. Catal. B Environ. 74 (2007) 53–62, https://doi.org/10.1016/j.apcatb.2006.12.015.

[31] M. Hinojosa-Reyes, S. Arriaga, L.A. Diaz-Torres, V. Rodríguez-González, Gas-phase photocatalytic decomposition of ethylbenzene over perlite granules coated with indium doped TiO_2, Chem. Eng. J. 224 (2013) 106–113, https://doi.org/10.1016/j.cej.2013.01.066.

[32] S.A. Awad, E.M. Khalaf, Improvement of the chemical, thermal, mechanical and morphological properties of polyethylene terephthalate–graphene particle composites, Bull. Mater. Sci. 41 (2018), https://doi.org/10.1007/s12034-018-1587-1.

[33] E.E. Hernández-Coronado, E.J. Ruiz-Ruiz, L. Hinojosa-Reyes, F.J. Beltrán, J. López-Gallego, M.Á. Gracia-Pinilla, M. Villanueva-Rodríguez, Effective degradation of cefuroxime by heterogeneous photo-Fenton under simulated solar radiation using α-Fe_2O_3-TiO_2, J. Environ. Chem. Eng. 9 (2021), https://doi.org/10.1016/j.jece.2021.106822.

[34] D. Magri, P. Sánchez-Moreno, G. Caputo, F. Gatto, M. Veronesi, G. Bardi, T. Catelani, D. Guarnieri, A. Athanassiou, P.P. Pompa, D. Fragouli, Laser ablation as a versatile tool to mimic polyethylene terephthalate nanoplastic pollutants: characterization and toxicology assessment, ACS Nano 12 (2018) 7690–7700, https://doi.org/10.1021/acsnano.8b01331.

[35] S. Dong, W. Cai, J. Xia, L. Sheng, W. Wang, H. Liu, Aggregation kinetics of fragmental PET nanoplastics in aqueous environment: Complex roles of electrolytes, pH and humic acid, Environ. Pollut. 268 (2021), 115828, https://doi.org/10.1016/j.envpol.2020.115828.

[36] L. He, Y. Dong, Y. Zheng, Q. Jia, S. Shan, Y. Zhang, A novel magnetic MIL-101(Fe)/TiO_2 composite for photo degradation of tetracycline under solar light, J. Hazard. Mater. 361 (2019) 85–94, https://doi.org/10.1016/j.jhazmat.2018.08.079.

[37] R. Nivetha, K. Gothandapani, V. Raghavan, G. Jacob, R. Sellappan, P. Bhardwaj, S. Pitchaimuthu, A.N.M. Kannan, S.K. Jeong, A.N. Grace, Highly porous MIL-100 (Fe) for the hydrogen evolution reaction (HER) in acidic and basic media, ACS Omega 5 (2020) 18941–18949, https://doi.org/10.1021/acsomega.0c02171.

[38] L. Han, H. Qi, D. Zhang, G. Ye, W. Zhou, C. Hou, W. Xu, Y. Sun, A facile and green synthesis of MIL-100(Fe) with high-yield and its catalytic performance, New J. Chem. 41 (2017) 13504–13509, https://doi.org/10.1039/C7NJ02975F.

[39] L. Ding, M. Li, Y. Zhao, H. Zhang, J. Shang, J. Zhong, H. Sheng, C. Chen, J. Zhao, The vital role of surface Brönsted acid/base sites for the photocatalytic formation of free $^{\bullet}$OH radicals, Appl. Catal. B: Environ. 266 (2020), https://doi.org/10.1016/j.apcatb.2020.118634.

[40] J. Chen, X. Zhang, X. Shi, F. Bi, Y. Yang, Y. Wang, Synergistic effects of octahedral TiO_2-MIL-101(Cr) with two heterojunctions for enhancing visible-light photocatalytic degradation of liquid tetracycline and gaseous toluene, J. Colloid Interface Sci. 579 (2020) 37–49, https://doi.org/10.1016/j.jcis.2020.06.042.

[41] P. Armando, V.B. Lunardi, F. Edi Soetaredjo, J.N. Putro, S.P. Santoso, C.J. Wijaya, J. Lie, W. Irawaty, M. Yuliana, H. Shuwanto, H. Abdullah, I.G. Wenten, S. Ismadji, Preparation of Fe-based MOFs composite as an adsorptive photocatalyst with enhanced photo-fenton degradation under LED light irradiation, Sustainability 14 (2022) 10685, https://doi.org/10.3390/su141710685.

[42] Y. Ma, Y. Lu, G. Hai, W. Dong, R. Li, J. Liu, G. Wang, Bidentate carboxylate linked TiO_2 with NH_2-MIL-101 (Fe) photocatalyst: a conjugation effect platform for high photocatalytic activity under visible light irradiation, Sci. Bull. 65 (8) (2020) 658–669, https://doi.org/10.1016/j.scib.2020.02.001.

[43] F. Zhang, Y. Jin, J. Shia, Y. Zhong, W. Zhua, M.S. El-Shall, Polyoxometalates confined in the mesoporous cages of metal-organic framework MIL-100(Fe): Efficient heterogeneous catalysts for esterification and acetalization reactions, Chem. Eng. J. 269 (2015) 236–244, https://doi.org/10.1016/j.cej.2015.01.092.

[44] M. Thommes, K. Kaneko, A.V. Neimark, J.P. Olivier, F. Rodríguez-Reinoso, J. Rouquerol, K.S.W. Sing, Physisorption of gases, with special reference to the evaluation of surface area and pore size distribution (IUPAC Technical Report, Pure Appl. Chem. 87 (2015) 1051–1069, https://doi.org/10.1515/pac-2014-1117.

[45] W. He, Z. Li, S. Lv, M. Niu, W. Zhou, J. Li, R. Lu, H. Gao, C. Pan, S. Zhang, Facile synthesis of Fe_3O_4@MIL-100(Fe) towards enhancing photo-Fenton like degradation of levofloxacin via a synergistic effect between Fe_3O_4 and MIL-100 (Fe), Chem. Eng. J. 409 (2021), https://doi.org/10.1016/j.cej.2020.128274.

[46] X. Liu, R. Dang, W. Dong, X. Huang, J. Tang, H. Gao, G. Wang, A sandwich-like heterostructure of TiO_2 nanosheets with MIL-100(Fe): A platform for efficient visible-light-driven photocatalysis, Appl. Catal. B: Environ. 209 (2017) 506–513, https://doi.org/10.1016/j.apcatb.2017.02.073.

[47] 44 Y. Xi, X. Zhang, Y. Shen, W. Dong, Z. Fan, K. Wang, S. Zhong, S. Bai, Aspect ratio dependent photocatalytic enhancement of $CsPbBr_3$ in CO_2 reduction with two-dimensional metal organic framework as a cocatalyst, Appl. Catal. B: Environ. 297 (2021), 120411, https://doi.org/10.1016/j.apcatb.2021.120411.

[48] M. Ahmad, S. Chen, F. Ye, X. Quan, S. Afzal, H. Yu, X. Zhao, Efficient photo-Fenton activity in mesoporous MIL-100(Fe) decorated with ZnO nanosphere for pollutants degradation, Appl. Catal. B: Environ. 245 (2019) 428–438, https://doi.org/10.1016/j.apcatb.2018.12.057.

[49] G.B. Dąbrowska, K. Janczak, A. Richert, Combined use of Bacillus strains and Miscanthus for accelerating biodegradation of poly(lactic acid) and poly(ethylene terephthalate), PeerJ 9 (2021), e10957, https://doi.org/10.7717/peerj.10957.

[50] M.C. Ariza-Tarazona, J.F. Villarreal-Chiu, J.M. Hernández-López, J. Rivera De la Rosa, V. Barbieri, C. Siligardi, E.I. Cedillo-González, Microplastic pollution reduction by a carbon and nitrogen-doped TiO_2: effect of pH and temperature in the photocatalytic degradation process, J. Hazard. Mater. 395 (2020), 122632, https://doi.org/10.1016/j.jhazmat.2020.122632.

[51] K.N. Fotopoulou, H.K. Karapanagioti, Degradation of various plastics in the environment, in: H. Takada, H. Karapanagioti (Eds.), Hazardous Chemicals Associated with Plastics in the Marine Environment. The Handbook of Environmental Chemistry 78, Springer, Cham, 2017, pp. 71–92, https://doi.org/10.1007/698_2017_11.

[52] A. Gok, Degradation pathway models of poly (ethylene-terephthalate) under accelerated weathering exposures, Case Western Reserve University, 2016. http://rave.ohiolink.edu/etdc/view?acc_num=case1449244610.

[53] F.J. Horne, J.J. Liggat, W.A. MacDonald, S.W. Sankey, Photo-oxidation of poly (ethylene terephthalate) films intended for photovoltaic backsheet, J. Appl. Polym. Sci. 137 (2020) 48623, https://doi.org/10.1002/app.48623.

[54] M.M. Ferreira, E.A. da Silva, F. Cotting, Vd.F.C. Lins, UV weathering and performance of a novel corrosion protective coating on steel made from recycled polyethylene terephthalate (PET), Corros. Eng. Sci. Technol. 56 (2020) 199–209, https://doi.org/10.1080/1478422X.2020.1836880.

[55] A. Uheida, H.G. Mejía, M. Abdel-Rehim, W. Hamd, J. Dutta, Visible light photocatalytic degradation of polypropylene microplastics in a continuous water flow system, J. Hazard. Mater. 406 (2021), 124299, https://doi.org/10.1016/j.jhazmat.2020.124299.